Materialia 15 (2021) 100988

Contents lists available at ScienceDirect

Materialia

journal homepage: www.elsevier.com/locate/mtla

Role of phosphate, calcium species and hydrogen peroxide on albumin protein adsorption on surface oxide of Ti6Al4V alloy

Ehsan Rahimi[a], Ruben Offoiach[a], Kitty Baert[b], Herman Terryn[b], Maria Lekka[a,c,*], Lorenzo Fedrizzi[a]

[a] Polytechnic Department of Engineering and Architecture, University of Udine, 33100 Udine, Italy
[b] Vrije Universiteit Brussel, Department of Materials and Chemistry, Research Group Electrochemical and Surface Engineering, Pleinlaan 2, 1050 Brussels, Belgium
[c] CIDETEC, Basque Research and Technology Alliance (BRTA), Po. Miramón 196, 20014 Donostia-San Sebastián, Spain

ARTICLE INFO

Keywords:
Albumin protein adsorption
Solution chemistry
Ti6Al4V
Inflammatory
Surface potential
corrosion initiation sites

ABSTRACT

Protein adsorption and its conformational arrangements on the surface of metallic biomaterials directly influence the biocompatibility and the degradation process during the implant lifetime. However, the presence of various species such as phosphates, calcium and hydrogen peroxide (H_2O_2) in the human body not only control the electrochemical interactions on the biomaterial surface but could also modify the protein adsorption process and its impact on the metal degradation. To this aim bovine serum albumin (BSA) protein adsorption, morphology, surface potential and its impact on the corrosion resistance of a Ti6Al4V alloy was investigated in different solutions, including a sodium chloride (NaCl), a phosphate-buffered saline (PBS) and Hank's physiological solutions. The results indicated that the alloy in PBS solution was more resistant to corrosion than that in Hanks' or NaCl solutions. Mott–Schottky analysis demonstrated that all solutions containing BSA and H_2O_2 had the highest donor charge carrier. Scanning electron microscopy (SEM) and surface potential images indicated that by changing the physiological solutions from NaCl to PBS and then to Hanks', the morphology of adsorbed BSA protein changed from a globular or unfolded shape to a large micronetwork and then to a fine micro-nanonetwork, accompanied by a gradual increase in the surface potential. Moreover, it was figured out that the BSA protein/substrate interface and the top surface of the BSA protein were susceptible to corrosion initiation owing to the different surface potentials and thus are preferable sites for the adsorption of corrosive counterions, e.g., Cl^-.

1. Introduction

The adsorption of plasma protein on material surfaces during biomaterial implantation in the human body has been a predominant research issue as it has a direct influence on the cellular response to the implanted biomaterials [1–4]. Protein adsorption, adhesion, distribution, and conformational changes on the surfaces of the implanted materials, as well as the interactions on bioactive sites, are among the first responses when a biomaterial is embedded into the physiological environment, which can, in turn, affect the biocompatibility of the implant [5]. The adsorption of proteins from a physiological medium is a dynamic and instantaneous process that can initially create a biofilm, which may then be rearranged or detached [6].

Protein adsorption on solid surfaces is a complex process with different interactions involving electrostatic, hydrophobic, van der Waals, and hydrogen bonding [7,8]. Both electrostatic attraction forces and hydrophobicity interactions have the highest impact on protein adsorption, which can be influenced by the surface properties and environmental conditions [7,8]. Moreover, the charge, concentration and hydrophobicity of the protein, as well as the pH, ionic strength, and agitation of the electrolyte, could control the adsorption mechanism [6,9].

Commercially pure titanium (CP-Ti) and Ti6Al4V alloys have been widely used in orthopaedic, dental, and cardiovascular devices owing to their excellent mechanical properties, including respectable fatigue strength, low elastic modulus, high corrosion resistance, and biocompatibility [10]. However, after implantation and depending on the exposure time, metallic implants can have poor osseointegration and osteoconductivity, along with aseptic loosening and metal ion release [10,11]. All these factors can lead to implant rejection.

Cathodic and anodic electrochemical reactions on the oxide films of titanium and its alloys in physiological media lead to the reduction of oxygen, resulting in some partial reactions with radicals and hydrogen peroxide (H_2O_2) [12,13]. In particular, it has been demonstrated, by electrochemical and immersion tests, that the presence of H_2O_2 and al-

* Corresponding author at: CIDETEC, Basque Research and Technology Alliance (BRTA), Po. Miramón 196, 20014 Donostia-San Sebastián, Spain
E-mail addresses: rahimi.ehsan@spes.uniud.it (E. Rahimi), ruben.offoiach@uniud.it (R. Offoiach), kitty.baert@vub.be (K. Baert), herman.terryn@vub.be (H. Terryn), mlekka@cidetec.es (M. Lekka), lorenzo.fedrizzi@uniud.it (L. Fedrizzi).

https://doi.org/10.1016/j.mtla.2020.100988
Received 17 October 2020; Accepted 12 December 2020
Available online 24 December 2020

bumin has a synergistic effect in increasing the corrosion rate of Ti6Al4V alloys in NaCl electrolyte [12]. The activation of inflammatory cells, especially macrophages and neutrophils, which are the first cells adsorbed on the implant surface, and oral bacteria trigger the production of reactive oxygen species (ROS) and extracellular H_2O_2 (μM–mM) with wound healing performance [11,13]. Likewise, the constant formation of ROS at the oxide layer/protein interface provides favourable conditions for metal ion release and aseptic loosening of the implant [14].

The composition, amount, size, and conformational arrangement of the protein-adsorbed layer are strongly dependent on the surface energy, topography, hydrophobicity, and chemical composition of the oxide layer of the metallic implants [9]. Indeed, the structure and properties of the oxide layer (single or complex oxide layer with homogeneous or heterogeneous distribution) on metallic surfaces could play a decisive role in the protein adsorption mechanism. The outstanding corrosion resistance and high biocompatibility of titanium and its alloys are related to the thin passive film on the material's surface, especially during contact with physiological media [15]. J. P. Bearinger et al. studied extensively the oxides formation on the surface of both commercially pure Ti and Ti6Al4V under polarization conditions in physiological media showing that the chemical composition distribution, the microstructure and the electronic properties (n-type or p-type semiconductor characteristics) of the formed oxides are influenced by the applied potential and the chemical composition of the physiological medium [16]. The characteristics of this passive film can significantly influence also the protein adsorption or desorption as well as its conformational arrangements. The kinetics and thermodynamics of adsorption or desorption of proteins, as well as their conformational rearrangements, including denaturation, spreading, and dissolution on solid surfaces, have been studied by researchers using a variety of techniques, including Raman [17], UV-visible [18], infrared (IR) [10], and sum-frequency generation (SFG) spectroscopies [19], X-ray photoelectron spectroscopy (XPS) [5,15], ellipsometry [20,21], quartz crystal microbalance (QCM) [22], atomic force microscopy (AFM) [4,23,24], and electrochemical measurements [25–28].

Recently, scanning Kelvin probe force microscopy (SKPFM) was employed to determine the surface potential or work function energy (WFE) of a material at the nano or atomic scale in a vacuum or air atmosphere [29]. In this method, a conductive tip scans the considered surface with DC and AC applied bias voltages between the tip and sample surface. External bias feedback (surface potential difference) is used to match the potential of the tip with respect to the sample surface, which triggers nullification of the tip-sample electrostatic interaction [30]. Materials with a high WFE and surface potential reveal a more stable electronic state that restricts valence electrons from participating in electrochemical reactions [31,32]. The main advantage of SKPFM is that it is contact-less as compared to the conductive AFM (C-AFM) method, which requires contact with the sample surface. SKPFM is thus appropriate for characterising the electronic properties of soft organic and biological samples [33]. As reported by Sinensky et al. [34], avidin molecules behaved with a higher surface potential with respect to the substrate at neutral pH with an isoelectric point (IEP) of 10.5. Leung et al. [35] showed that the positive surface potential of avidin compared to the silicon matrix is due to the more negative charge of the substrate surface.

The solution chemistry, type and concentration of ions and the pH can alter the distribution of the charged and polar residues in the protein structure and the IEP, which directly affect the electrostatic properties of the protein [19]. Consequently, the surface potential distribution on heterogeneous metal surfaces with various organic materials (proteins, DNA, etc.) can be affected by the physiological environment composition and, in turn, determine the surface conductivity directly correlated to the electrochemical activity.

In this study, we evaluated the effect of different simulated physiological solutions, including a 0.9%wt. NaCl solution, phosphate-buffered solution (PBS), and Hanks' solution, along with an inflammatory condition simulated by the addition of hydrogen peroxide (H_2O_2), on bovine serum albumin (BSA) protein adsorption, conformational arrangement, and surface potential distribution on a Ti6Al4V alloy. A direct comparison of the three most used solutions to simulate body fluids, highlighting the role of the most important ions or inorganic species of the solutions, on the corrosion resistance and on the passive film formation on the Ti6Al4V alloy is performed for the first time also in presence of compounds like BSA and H_2O_2 simulating inflammatory conditions. A multi-characterisation approach was followed using electrochemical measurements, especially Mott–Schottky (MS) analysis, scanning electron microscopy (SEM), XPS, AFM, and SKPFM to reveal and establish the BSA protein interaction mechanism with the above mentioned species and its role in corrosion phenomena occurring on a heterogeneous surface. MS analysis is used to reveal the semiconductive properties of the passive film and correlate them to the degradation mechanisms.

2. Material and methods

2.1. Sample preparation

Specimens with surface areas of 5 cm^2 have been used for electrochemical measurements and specimens with surface areas of 0.8 cm^2 have been used microstructural characterisation and AFM and SKPFM measurements. All specimens were cut from a bar of Ti6Al4V ASTM F1472 alloy which chemical composition (wt.%) was 6.25 Al, 0.065 C, 0.23 Fe, 0.003 H, 0.01 N, 0.185 O, 4.45 V, 0.001 Y, Ti (balance). The samples were mechanically ground and polished to a mirror-like surface, washed with ethanol, ultrasonicated in acetone for 30 min, and finally dried by air blowing before characterisation. All samples for surface analysis and microscopic measurements were stored in a desiccator at room temperature.

2.2. Electrolyte and electrochemical measurements

The electrochemical behaviour of the Ti6Al4V alloy was studied in different physiological environments to reveal the effect of the solution chemistry on protein adsorption, morphology, surface potential, donor density, and corrosion initiation sites on the oxide layer of the Ti6Al4V alloy. Thus, NaCl, PBS (different salts were purchased from Sigma-Aldrich), and Hanks' solutions (H 8264, Sigma-Aldrich) were prepared as shown in Table 1. To investigate the electrochemical interaction and morphological arrangements of BSA protein on the Ti6Al4V alloy surface, 1 g L^{-1} of BSA protein (lyophilised powder; ≥96% agarose gel electrophoresis, Sigma-Aldrich) was dissolved in the abovementioned solutions and the pH was adjusted to approximately 7.4. 100 μM H_2O_2 (PanReac Applichem, 30% w/v) was also added to some solutions to simulate inflammation conditions [13].

Electrochemical measurements were carried out using an Avesta cell according to the method of Qvarfort [36] and a conventional three-electrode electrochemical cell to reduce or eliminate the crevice corrosion around the specimen holder and to control the temperature at 37 °C. The measurements were conducted using an AUTOLAB PGSTAT 30 potentiostat, a $Ag/AgCl/KCl_{3M}$ electrode (+222 vs. SHE) as the reference electrode, and a platinum wire as the counter electrode. All electrochemical measurements were performed after 1-h immersion in the solutions to stabilise the open-circuit potential (OCP) and reach the steady-state condition. The potentiodynamic polarisation (PDP) measurements were carried out at a scan rate of 1 mV s^{-1} from cathodic to anodic potentials. Electrochemical impedance spectroscopy (EIS) measurements were performed in the frequency range of 100 kHz to 10 mHz by applying a sinusoidal excitation signal of ±10 mV. The electronic properties of the passive film on Ti6Al4V were investigated by MS analysis at 1 kHz frequency in the potential range from −1 to 1 V vs. Ag/AgCl with an amplitude of ±10 mV in all selected solutions.

Table 1
Chemical composition and parameters of the NaCl, PBS and Hanks' solutions.

Solution	$CaCl{\cdot}2H_2O$ ($g{\cdot}L^{-1}$)	$MgSO_4$ ($g{\cdot}L^{-1}$)	KCl ($g{\cdot}L^{-1}$)	KH_2PO_4 ($g{\cdot}L^{-1}$)	$NaHCO_3$ ($g{\cdot}L^{-1}$)	NaCl ($g{\cdot}L^{-1}$)	Na_2HPO_4 ($g{\cdot}L^{-1}$)	pH	Temperature (°C)
NaCl	–	–	–	–	–	9	–	7.4	37
PBS	–	–	0.2	0.2	–	8	1.15	7.4	37
Hanks	0.185	0.097	0.4	0.06	0.35	8	0.047	7.4	37

2.3. Microstructure characterisation and AFM/SKPFM measurements

The protein adsorption on the passive film of the Ti6Al4V alloy was studied using SEM and AFM/SKPFM techniques. The microscopy observations were performed after polarising the specimens to +0.2 V vs. Ag/AgCl (in the passivity region) immersed in different physiological environments with or without the addition of BSA protein or H_2O_2 for 1 h. The SEM was a SM-7610FPlus instrument (JEOL) equipped with an Oxford X-MAX20 energy-dispersive X-ray spectrometer (EDXS) and the observations have been performed at a working distance of 15 mm, an accelerating voltage of 5 kV, and secondary electron (SE) mode. The AFM device was a Nanoscope IIIa Multimode with an n-type doped silicon pyramid single-crystal tip coated with PtIr5 (SCM-Pit probe). The surface potential images were captured in dual-scan mode. In the first scan, topography data were obtained using tapping mode, and in the second scan, the surface potential was detected by lifting the tip 100 nm. Topographic and surface potential images were obtained in air atmosphere at 27 °C with an approximate relative humidity (RH) of 28%, a pixel resolution of 512 × 512, zero-bias voltage, and a scan frequency rate of 0.2 Hz.

The histogram and power spectral density (PSD) analysis based on the multimodal Gaussian distributions (MGD) and fast Fourier transform (FFT), respectively, were used to interpret the surface potential on the heterogeneous surface affected by the differential BSA protein shape, morphology, and WFE. The histogram and PDS analysis were performed according to the procedure followed in previous works [37–39].

2.3. X-ray photoelectron spectroscopy (XPS)

The chemical composition of the surface layer on Ti6Al4V was analysed by a PHI-5000 Versaprobe II (Physical Electronics) using a monochromatic Al Kα X-ray source (1486.71 eV photon energy) and a spot diameter of 100 μm to measure surface compositions up to ca. 10 nm in depth. The irradiation power of the X-ray beam was 25 W. The kinetic energy of the photoelectrons was measured with a take-off angle of 45°. The vacuum in the analysis chamber was approximately 1×10^{-9} Torr. The XPS results were analysed using the PHI Multipak software (V9.0). High-resolution scans of C 1s, N 1s, O 1s, Ti 2p, Al 2p, P 2p, and Ca 2p were obtained with a pass energy of 23.5 eV and a 0.05 eV energy step size.

3. Results and discussion

3.1. PDP and EIS measurements of the complex surface layer

The influence of phosphate and calcium species, as well as of BSA protein and H_2O_2, on the resistivity of the oxide layer was investigated, and the BSA protein adsorption and conformational changes during interaction with the oxide layer on the Ti6Al4V alloy were evaluated. The PDP curves of the Ti6Al4V alloy in NaCl, PBS, and Hanks' solution are shown in Fig. 1a–c, respectively. The key electrochemical parameters such as the corrosion potential (E_{corr}) and corrosion current density (i_{corr}) calculated by Tafel extrapolation, along with passive current density (i_{pass}), are shown in Fig. 1d–f, respectively.

The addition of 1 g L^{-1} of BSA protein led to a decrease in E_{corr} (of about 80 mV) and a slight increase in i_{corr} (of about 0.04 μA cm^2) in all three physiological solutions. Likewise, a slight decrease in the cathodic current was detected upon adding BSA protein. The BSA protein could have inhibited the cathodic reactions (hydrogen or oxygen evolution) by covering the active sites on the heterogeneous surface with chemisorbed bonds [13,40,41]. An increase in both the passivity region and i_{pass} (of about 1.5 μA cm^2) in the presence of BSA protein was observed in the PDP curves. This can be attributed to the BSA protein molecules or complexes that control the kinetics of metal ion release and reduction reactions [42]. A similar effect has been observed for other implant materials, such as CoCrMo and stainless steel 316L, in various physiological solutions [2,6,43]. This mechanism can be explained by the external donation of hydrogen atoms through protonation to protein amino groups on the Ti oxide layer that could trigger protein adsorption and covering according to the following equation [40]:

$$Ti - OH + NH_3^+ \rightarrow Ti - OH_2^+ : NH_2 - R \quad (1)$$

Moreover, the i_{corr} of the Ti6Al4V alloy in the PBS media presented a slightly lower value than that in the Hanks' or NaCl solutions ($0.18_{NaCl} > 0.14_{Hanks} > 0.12_{PBS}$ $\mu A\ cm^{-2}$), as presented in Fig. 1e. It can be supposed that the phosphate species, which has a higher concentration in PBS than in Hanks' solution, can adsorb onto the TiO_2 oxide layer with the formation of a thin and compact film, thus reducing the activity or charge transfer through the TiO_2 oxide layer [42,44]. In fact, the Ti–OH bond is replaced by a Ti–OP bond, changing the basic hydroxyl group into $H_2PO_4^-$ and/or $HPO_4^{2-}$and leading to the formation of a strong complexation bond with Ti on the passive film [41]. When a Ti6Al4V alloy is immersed in Hanks' solution, the first stage is the formation of calcium-phosphate, which occurs by preferential adsorption of phosphate ions on the TiO_2 oxide layer [45]. The growth of the TiO_2 oxide layer is accompanied by hydration, creating TiOH groups at the oxidised surface, which leads to the binding of calcium ions (Ca^{2+}) to the hydrated oxide layer or electrostatic interaction with O^{-1} [25,46].

The Ti6Al4V alloy showed a very small active/passive peak in the PDP curves obtained in both the PBS and Hanks' solution environments owing to the formation of Ti^{3+} [12]. The addition of BSA protein to PBS and Hanks' solution led to a decrease in the active/passive potential peaks (inserted images in Fig. 1b and c) from 69 to 1 mV vs. Ag/AgCl and from 56 to −9 mV vs. Ag/AgCl, respectively.

The addition of H_2O_2 to all environments led to an increase in both E_{corr} (of about 200 mV) and i_{corr}, (of about 0.2 $\mu A\ cm^{-2}$) as shown in Fig. 1d and e, respectively. The most marked effect was the increase in i_{pass} compared to that of the base solutions. Because H_2O_2 has a high standard electrode potential (1.54 V vs. SCE), its reduction provides a more positive E_{corr} and higher cathodic current densities [12]. According to previous studies [47–50], H_2O_2 has a negative effect on the corrosion resistance of Ti implant materials, creating rough surfaces because of the selective dissolution of the β-phase. Under harsh inflammatory conditions, which were simulated by adding BSA+H_2O_2 to the three different solutions, a decrease in the cathodic current density and E_{corr} with respect to the addition of only H_2O_2 was detected owing to the role of BSA protein as a complex agent with oxides or corrosion products on the TiO_2 film.

Fig. 2a–c represent the Bode phase and Bode magnitude diagrams of the Ti6Al4V alloy in NaCl, PBS, and Hanks' solutions, respectively. The Ti6Al4V samples in the three physiological solutions show only a one-time constant in the frequency range of 0.01–100 kHz. The fitting process of the EIS measurements was carried out using the ZView software package and the results are presented in Table 2. The equivalent

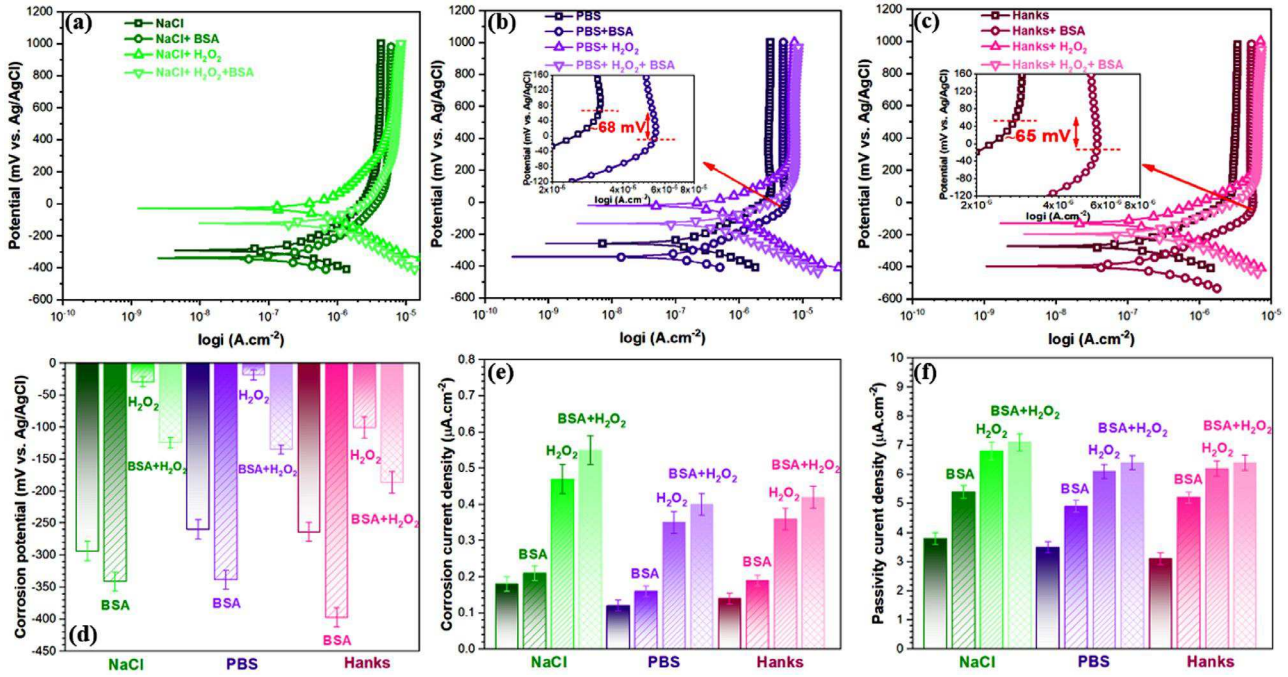

Fig. 1. PDP plots of Ti6Al4V alloy after 1-h immersion in (a) NaCl, (b) PBS, and (c) Hanks physiological solutions with the addition of either BSA or H_2O_2 or both at 37 °C, pH 7.4, and aerated conditions, (d) Ecorr, (e) icorr and (f) ipassive values as calculated from the PDP curves.

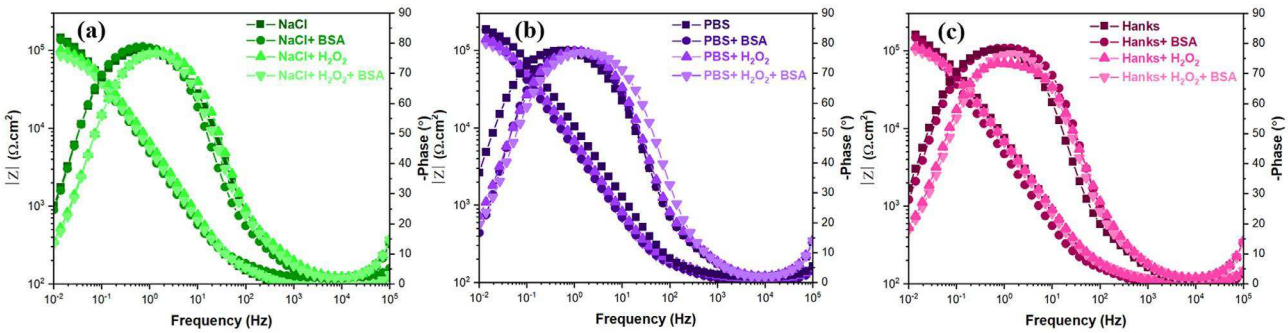

Fig. 2. EIS spectra of Ti6Al4V alloy after 1-h immersion in (a) NaCl, (b) PBS, and (c) Hanks physiological solutions with the addition of either BSA or H_2O_2 or both at 37 °C, pH 7.4, and aerated conditions.

Table 2
Fitting data obtained from EIS measurements in Fig. 2 using an R(RCPE) equivalent electrical circuit.

Condition	R_s (Ω.cm^2)	R_{ct} (KΩ.cm^2)	CPE_{dl} (μF S^{-1} cm^{-2})	n_{ads}
NaCl				
NaCl	86 ± 5	159 ± 6	34 ± 2	0.92 ± 0.02
NaCl+ BSA	128 ± 5	147 ± 10	29 ± 3	0.91 ± 0.02
NaCl+ H_2O_2	87 ± 8	104 ± 6	30 ± 4	0.88 ± 0.01
NaCl+ BSA+ H_2O_2	95 ± 6	91 ± 12	35 ± 6	0.88 ± 0.02
PBS				
PBS	119 ± 8	221 ± 8	35 ± 4	0.90 ± 0.02
PBS + BSA	106 ± 4	200 ± 4	20 ± 8	0.88 ± 0.03
PBS + H_2O_2	109 ± 3	151 ± 8	31 ± 2	0.89 ± 0.02
PBS + BSA+ H_2O_2	118 ± 5	129 ± 5	28 ± 6	0.88 ± 0.03
Hanks				
Hanks	126 ± 4	212 ± 11	38 ± 4	0.89 ± 0.02
Hanks + BSA	104 ± 7	168 ± 10	25 ± 7	0.90 ± 0.01
Hanks + H_2O_2	115 ± 8	119 ± 8	29 ± 3	0.88 ± 0.02
Hanks + BSA+ H_2O_2	107 ± 5	106 ± 11	28 ± 3	0.86 ± 0.02

electrical circuit includes R_s as the solution resistance, R_{Com} as the resistance of the complex layer (protein–passive film), and CPE_{dl} as the constant-phase element of the double layer or the complex layer. CPE is used instead of a capacitor because the capacitive elements have non-ideal behaviour owing to surface roughness and heterogeneity during BSA molecule or complex interactions [43]. According to the literature [41,51], a Ti alloy is composed of two oxide layers, with a porous outer layer and a barrier inner layer. However, the outer layer in this study was not clear and integrated into a complex layer with phosphate, calcium-phosphate, protein, and protein–metal species or in the form of an inhomogeneous region.

The Bode modulus diagrams in NaCl solutoin, PBS, and Hanks' solution revealed that the inflammatory condition simulated by BSA proteins and H_2O_2 led to a slight decrease in the corrosion resistance of the Ti6Al4V sample. It should be considered that BSA strongly adsorbs onto the TiO_2 oxide layer by chemisorption through a carboxylate-amino acid group with electrostatic or hydrophobic interactions and that it controls the kinetics of electrochemical reactions [12]. Therefore, the Ti6Al4V samples in the BSA/H_2O_2 solutions showed the lowest corrosion resistance and were more susceptible to metal ion release. Likewise, a slight shift in the magnitude of the phase angle from 80° to 75° can be seen in the BSA/H_2O_2 integrated inflammatory condition owing to the decrease in the dielectric properties and their effect on the capacitance of the oxide layer.

3.2. Mott–Schottky analysis of complex surface layer

The semiconductor characteristics of the passive film on Ti6Al4V alloy and the donor or acceptor density were measured in the different physiological environments by the capacitance (space charge region and Helmholtz double-layer)/solution interface with respect to the applied potential at 37 °C, pH 7.4. The MS analysis is explained by the following equation [52]:

$$\frac{1}{C_{SC}^2} + \frac{1}{C_H^2} = \pm\frac{2}{\varepsilon\varepsilon_0 e N_{d\ or\ a}}\left(E - E_{fb} - \frac{kT}{e}\right), \tag{2}$$

where C_{SC} is the space charge capacitance, C_H is the capacitance of the Helmholtz double-layer, E is the applied potential, ε is the dielectric constant of the passive film, ε_0 is the vacuum permittivity (8.854×10^{-14} F cm^{-1}), e is the electron charge (1.6×10^{-19} C), N_d is the donor density, N_a is the acceptor density, E_{fb} is the flat band potential, and k and T are the Boltzmann constant and absolute temperature, respectively. As mentioned above, the C^{-2} magnitude is a reflection of the total capacitance value at the oxide surface/electrolyte interface into the space charge region, the Helmholtz layer, and the non-uniform or heterogeneous protein adsorbed layer (only in the protein environment). Because the physicochemical interactions of protein molecules such as adsorption and detachment are dynamic processes, the different potential sweeping on MS can significantly affect these interactions [53,54]. Hence, we can state that the major part of the C^{-2} magnitude is related to the space charge capacitance of the oxide layer.

According to previous studies [12,25,51,55], the passive film on Ti and its alloys is a mixture of TiO (close to the metallic substrate), TiO_2, and Ti_2O_3 (on the top of the passive film), which can affect protein adsorption, conformational alternation, and electron transfer for electrochemical reactions. The low donor density value explains the electrochemical reactions at the TiO_2 passive film/solution interface, which can be inhibited by reducing the charge transfer. The intensity of donor density is related to the density of the oxygen vacancies or the interstitial distribution of Ti or Al in the passive film region [56]. Thus, the decrease in the formation rate and transfer velocity of oxygen vacancies along with Ti interstitials enhances the stability and protective behaviour of the passive film with low mass transfer [57]. As shown in Fig. 3, all three basic solutions demonstrated an increasing trend in the C^{-2} magnitude (decline in space charge region) at the approximate potential of 0 V vs. Ag/AgCl owing to the transfer from the active region to the passive region. The linear region with a positive slope represents the n-type character of the semiconductor properties of the passive film [55]. The BSA protein slightly decreased the C^{-2} magnitude in the potential range of −1 to 0.1 V vs. Ag/AgCl in all tested environments. After 0.1 V vs. Ag/AgCl, in the BSA protein environments, there was a slight decrease in the C^{-2} magnitude, which can be attributed to the effect of BSA protein adsorption on the passive film and especially on the distribution of charge carrier densities. To calculate the N_d value, ε was considered to be 80 in agreement with previous studies [58]. N_d was calculated by fitting a straight line on the positive slope into the following equation [59]:

$$\alpha = \frac{-2}{N_d\ e\varepsilon\varepsilon_0}, \tag{3}$$

where α is the slope in C^{-2} versus the applied potential. The results of the fitting process on the Mott–Schottky curves are shown in Fig. 3d.

Adding H_2O_2 triggered an increase in the C^{-2} magnitude in all three solutions and at all applied potentials. H_2O_2 in the presence of phosphate or calcium-phosphate could modify the TiO_2 oxide layer and thicken it [11]. Protein molecules with complex effects could damage the TiO_2 oxide layer during the interaction with H_2O_2, increasing the material degradation [9]. The adsorbed protein on TiO_2 oxide can shift the E_{fb} to more negative values and increase N_d owing to local alkalisation of the (hydr)oxide surface groups on TiO_2 [60]. In fact, the adsorbed layer of BSA proteins can strongly affect the space charge region, which is directly related to the charge carrier density in the conduction band [60]. The donor density of the film formed on the Ti6Al4V in the three tested base solutions follows the order PBS<Hanks's<NaCl in all conditions. Adding BSA and H_2O_2 in all tested environments increased N_d, as shown in Fig. 3d. As a result, we can state that both BSA protein and BSA/H_2O_2 environments provide a higher dissolution rate owing to the increase in the number of defect sites and the higher rate of mass transport through the oxide region, which decreases the protective properties in accordance with the PDP and EIS results.

Throughout the range of applied potentials, especially between −1 V and 0.1 V vs. Ag/AgCl, specimens immersed in Hanks' solution showed a higher C^{-2} magnitude than those immersed in PBS and the NaCl solution. This is due to the calcium-phosphate complex layer formed on the TiO_2 oxide layer, which acted as a protective layer that inhibited the electrochemical reactions and blocked the mass transportation of oxygen or reaction products on passive film [28]. Likewise, BSA proteins tended to bind with the calcium-phosphate complex layer. Moreover, the phosphate compounds absorbed on the passive film and formed metal–phosphate complexes, which led to a decrease in i_{corr} or acted as an anodic inhibitor, shifting E_{corr} to more positive values.

3.3. Protein–oxide surface complex analysis by XPS

A complementary study was carried out by XPS surface analysis to reveal the significant role of phosphate and calcium species, BSA protein adsorption, and H_2O_2 interaction on the complex oxide layer on the Ti6Al4V alloy. The individual high-resolution spectra of elements are shown in Fig. 4 to highlight the the BSA protein adsorption and the H_2O_2 influence on the metal ion release and chemical composition distribution of the surface layer. Moreover, the element content distribution in the surface layer calculated from XPS results is shown in Fig. 4h. Two separate Ti peaks were detected on the Ti spectrum at binding energies of 464.8 ± 0.4 eV and 459.1 ± 0.8 eV, which are attributed to Ti^{4+} $2p_{1/2}$ and Ti^{4+} $2p_{3/2}$, respectively, in form of TiO_2 oxide [61]. Likewise, at a binding energy of 74.8 ± 0.6 eV, a sharp peak of the Al 2p spectrum was distinguished for the Al oxide [62]. The O 1s spectrum showed two dominant individual peaks that originated from oxide (O^{2-}) at 530.4 ± 0.8 eV and hydroxide or hydroxyl groups at 532.1 ± 0.4 eV arising from metal oxides and oxidised surface carbon [63]. The main content of the C spectrum originated from airborne carbon or contamination. According to previous studies [15,61], BSA

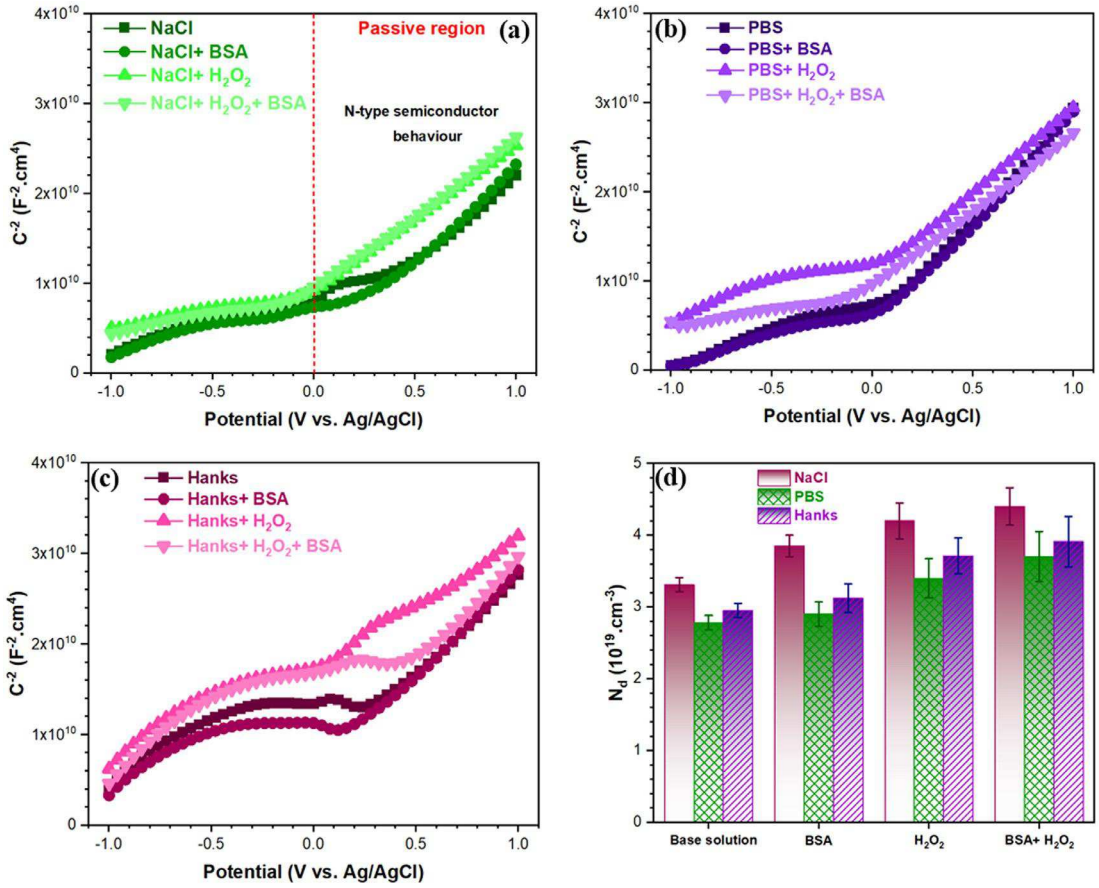

Fig. 3. Mott-Schottky analysis of Ti6Al4V alloy after 1-h immersion in (a) NaCl, (b) PBS, and (c) Hanks physiological solutions with the addition of either BSA or H_2O_2 or both at 37 °C, pH 7.4, and aerated conditions, (d) Donor carrier density in the passive film of Ti6Al4V alloy in the different physiological solutions.

protein is included in CO–NH peptides and in amino ($–NH_2$) and carboxyl (–COOH) groups. Thus, the C 1s peaks can be deconvoluted into three peaks at 284.5 ± 0.9 eV, 285.8 ± 0.8 eV, and 287.7 ± 0.9 eV, which are related to mainly C–C and C–H bonds, peptidic residues or C–O and C–N bonds, and N–C=O bonds, respectively [4,64]. Therefore, we can conclude that the higher C and N intensity peaks on the surface layer in all BSA solutions are due to BSA protein adsorption on the surface oxide. Ca spectrum peaks only appeared in Hanks' basic solution with two individual peaks at 347.6 ± 0.1 eV and 351.6 ± 0.2 eV, which are attributed to Ca^{2+} $2p_{3/2}$ and Ca^{2+} $2p_{1/2}$, respectively [65]. P spectrum peaks (P 2p3 peak) were well distinguished for PBS and Hanks' basic solution at a binding energy of 133.6 ± 0.5 eV [66].

By changing the solution chemistry from NaCl to PBS and Hanks' solutions, the Ti and Al spectra represented the same approximate Ti and Al contents on the surface layer, whereas the O spectrum increased on the surface oxide (Fig. 4h). However, with the addition of BSA protein to the three basic solutions, the amount of Ti on the surface oxide decreased and finally reached the lowest value in BSA+H_2O_2-containing solutions. However, the Al in the PBS+BSA solution showed a lower value than that in PBS, and again the content increased slightly in the PBS+BSA+H_2O_2 solution owing to the preferential dissolution of Ti [62]. A higher amount of Ti on the surface layer in both PBS and Hanks' solutions under BSA and BSA+H_2O_2 conditions was observed in comparison with the NaCl solution. Likewise, a decrease in the P and Ca contents by adding BSA and BSA+H_2O_2 to PBS and Hanks' solutions was observed. Comparing the three base solutions with BSA protein, the C and N contents followed the order NaCl > Hanks' > PBS. The C and N contents in the surface layer increased by adding H_2O_2 to the solutions containing BSA, indicating higher protein adsorption [62]. As a result, for all solutions with BSA+H_2O_2, the lowest Ti and Al contents and the highest C and N contents were observed. This is because H_2O_2 as an oxidising agent leads to the formation of a TiOOH defective complex or a H_2O_2–TiO_2 complex, which enhances the Ti and Al release process, especially from phosphate and calcium complexes that are bonded to Ti oxides [62,67].

In the PBS environment, HPO_4^{2-} and $H_2PO_4^-$ are dominant species that can easily adsorb onto TiO_2 oxide to form a thin phosphate-complex film. However, CaO and Na_3PO_4 or Na_2HPO_4 in Hanks' media tend to adsorb onto the TiO_2 oxide [66]. According to previous studies, we can deduce that the presence of Ca 2p3 at a binding energy of 347.6 eV is attributed to $CaHPO_4$ [68], whereas P 2p3 at a binding energy of 133.6 eV originates from HPO_4^{2-} or Na_2HPO_4 [69]. Therefore, the thin and rich layer of phosphate species formed in the PBS solution on the TiO_2 oxide offers better protection, hindering the release of Ti and Al ions or blocking the mass transport as compared to the NaCl and Hanks' solutions with $CaHPO_4$ [42]. The BSA protein in the NaCl solution had a higher adsorption rate than that in PBS and Hanks' solutions, which is related to the competition between the protein and the phosphate and calcium species. However, it should be noted that both BSA molecules and phosphate species have negative zeta potentials [2]. In fact, the phosphate and calcium species are smaller and move faster, thus bonding to the surface oxide better than the large protein molecules. This decreases the amount of protein on the surface layer due to the shielding or repulsing of protein molecules.

Likewise, the PBS solution showed slightly lower C and N contents (adsorbed proteins) than the Hanks' solution arising from the surface chemistry and electronic properties of the adsorbed phosphate species (discussed in the next section). Therefore, the formation of metal–

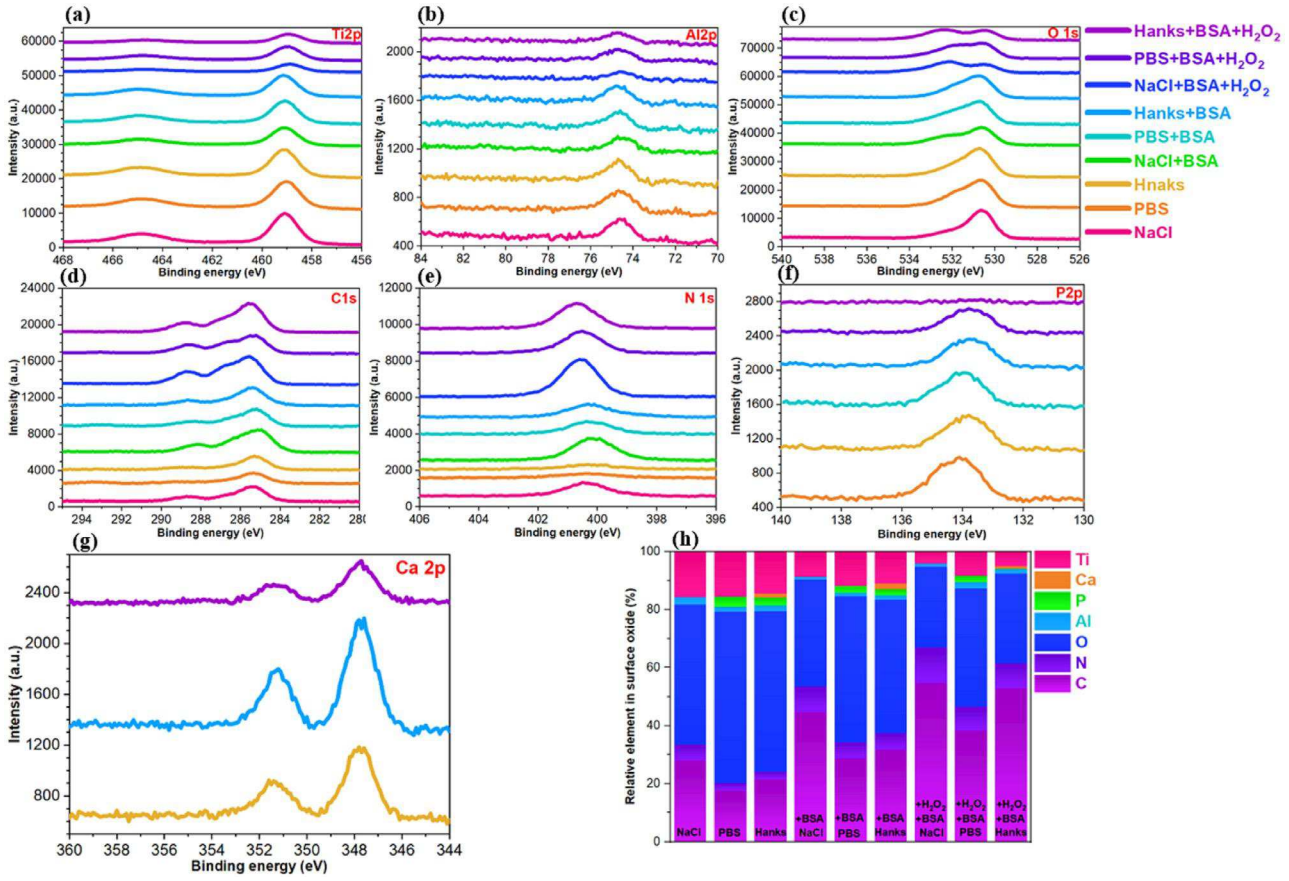

Fig. 4. XPS spectra of (a)Ti 2p, (b) Al 2p, (c) O 1s, (d) C 1s, (e) N 1s, (f) P 2p, and (g) Ca 2p electron energy regions on Ti6Al4V alloy after polarising at 0.2 V vs. Ag/AgCl for 1-h in NaCl, PBS, and Hanks solutions with or without BSA and H_2O_2, (h) Relative % of elements in the surface oxide calculated from XPS spectra.

protein complexes and not compact films is more probable on the surface layer in the Hanks' solution. Consequently, the higher the i_{corr} value, the lower the resistance to charge transfer. The higher density of charge carriers on the Ti surface oxide in NaCl solution is attributed to the high amount of adsorbed BSA protein on the surface oxide, which can lead to protein–metal complex detachment. A schematic representation of the different phenomena occurring on the surface of the Ti alloy immersed in different environments is shown in Fig. 5.

3.4. Surface potential and protein conformational arrangement

3.4.1. Analysis of the as-polished alloy

The heterogeneous surface of Ti6Al4V with α- and β-phases during exposure to the simulated environment can show different adsorption mechanisms of the various ions and protein species, protein conformations, and metal ion release processes. This is because the oxide layer on the different metal phases could have different chemical compositions, nanometric roughness, and WFEs with occupied and unoccupied densities of state, which can control the abovementioned parameters [70]. Therefore, SKPFM measurements were used to measure and correlate the morphology and surface potential of individual α- and β-phases according to different adsorption contents of protein and metal ion species.

Fig. 6 shows the topography and surface potential, respectively, of the air-formed passive film on the as-polished surface of the Ti6Al4V alloy. The surface potential image clearly distinguishes the α- and β-phases as separate regions with different WFEs as the nobility criterion. The diverse nobility of the α- and β-phases is related to the different elemental distributions and WFEs. According to the literature [71,72], the β-phase, which has a higher vanadium content, has a higher relative surface potential and acts as a nobler phase than the α-phase, which has a higher aluminium content. Vanadium has a higher WFE, 4.3 eV, in comparison to aluminium, which has a WFE of 4.26 eV in the polycrystalline condition [73]. According to EDX analysis, the β-phase contained 13.38% V and 4.79% Al, whereas the α-phase contained 2.28% V and 6.87% Al. Therefore, the α- and β-phases have different tendencies to transfer the valance electrons to electrochemical reactions at the passive film/solution interface, which in turn leads to a microgalvanic driving force for corrosion attack with active (anode) and noble (cathode) sites. Al and V ions released from Ti6Al4V surfaces can diminish normal bone healing processes, which leads to a negative effect on osteoblast cell behaviour [74]. It must be noted that vanadium stabilises the β-phase, and its oxide layer is harmful to the human body [51].

3.4.2. Effect of BSA protein under polarisation in different environments

The SKPFM and SEM micrographs of the Ti6Al4V specimens after 1-h polarisation at 0.2 V vs. Ag/AgCl in the three base solutions containing BSA protein at 37 °C are shown in Fig. 7. The presence of BSA protein in both the PBS and Hanks' solution led to a particular conformational arrangement of BSA protein with a fibrillar or network morphology on the surface layer in comparison with the NaCl solution, as shown in Fig. 7b and c. In the NaCl solution, individual α- and β-phases were detected with a new Volta potential distribution (Table 3), with no evidence of protein cluster morphology, as observed in PBS and Hanks' conditions. In PBS and Hank's solutions, no differences between the α- and β-phases could be distinguished and the BSA was adsorbed on the surface in the form of a dense network or cluster shape, as shown in both the SKPFM maps (darker regions) and SEM images. Additionally, two separate regions were detected, including protein-enriched regions and matrices (including both α- and β-phases), which were deconvoluted in the form of bimodal peaks in the histogram curves in Fig. 8a. The pro-

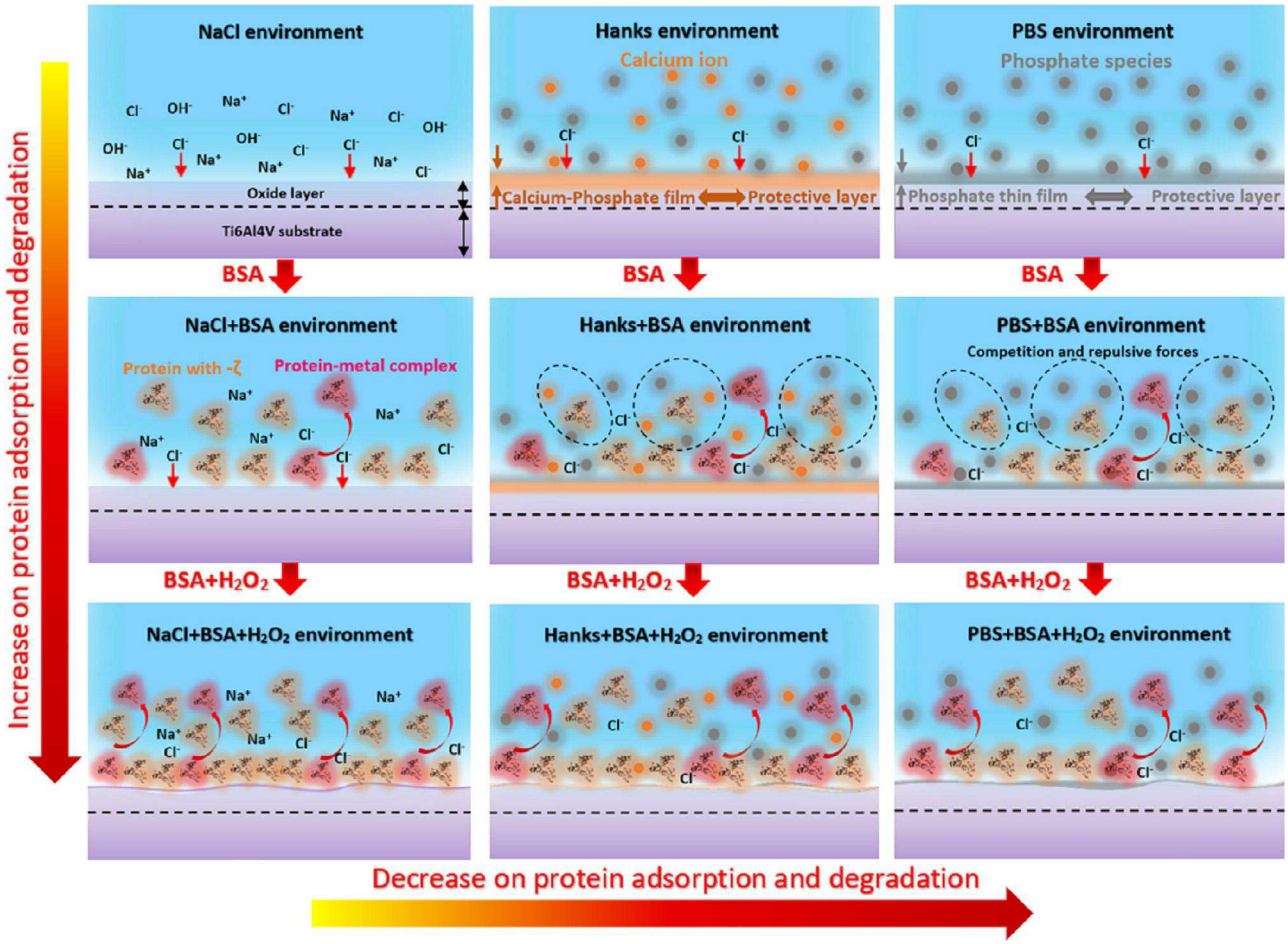

Fig. 5. Schematic representation of the role of the different species present in the tested environments and their influence on the BSA protein adsorption on the surface of Ti6Al4V and metal ion release.

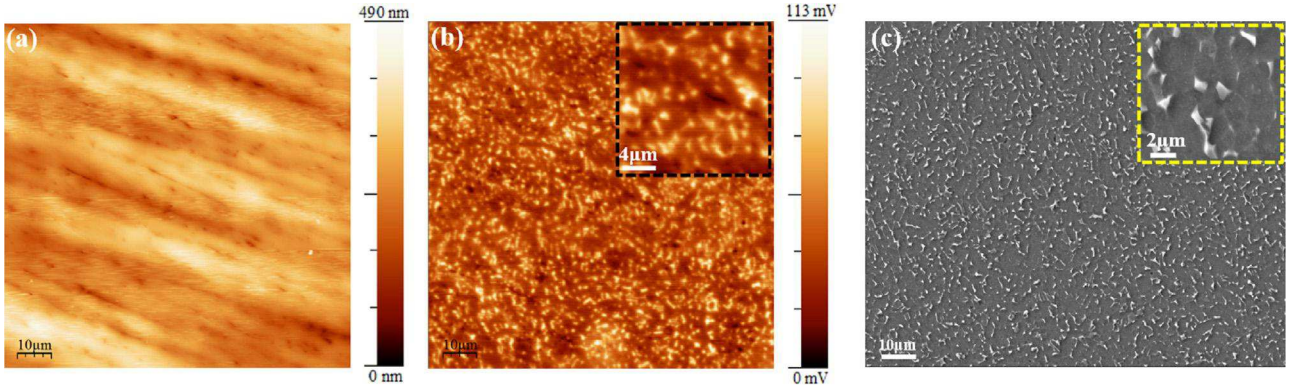

Fig. 6. (a) topography and (b) surface potential maps of polished Ti6Al4V alloy, (c) FESEM image of etched Ti6Al4V alloy.

tein enrichment region in PBS solution clearly exhibits a low surface potential or surface charge (as a criterion for electronic conductivity), with a mean value of 40.5 mV, as compared to the matrix or passivated film at 52.2 mV (Table 3). According to the literature [18], BSA protein (known as a low-conductive protein) exhibits low charge transport or electronic transport (ET) efficiency in comparison with other proteins such as azurin and bacteriorhodopsin (BR), with a high ET bias bandgap in the current–voltage curve (*I–V*).

The electrostatic surface potential of proteins and DNA molecules is governed by the surrounding surface charge and isoelectric point (IEP) [35,75]. The IEP is defined as the degree of the relative proton affinity of a molecule, which has an opposite correlation with the electronegativity. Additionally, the pH value, which is a measure of the protein surface charge, has a minimum value that can be defined as IEP [19]. Consequently, it can be said that the BSA protein with a fibrillar or network morphology has a low surface potential, which represents a low isoelectric point (~5.4 and ~5.2 for theoretical estimated and bulk measured, respectively [6,19]), which can affect the concentration of the charge carriers at the atomic and molecular levels of the BSA structure. The conformational or structural pattern changes of a protein molecule from globular to a network morphology is related to the chemical properties of the substrate, and migratory parameters lead to

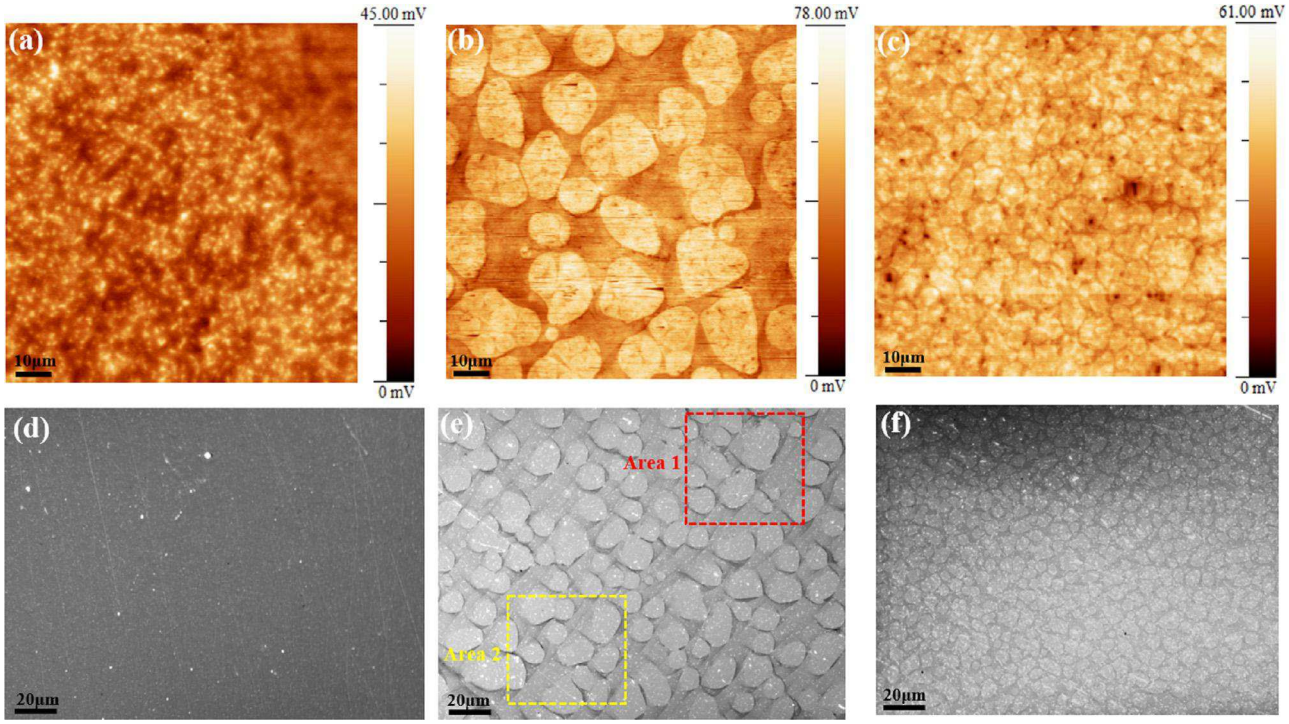

Fig. 7. Surface potential maps and SEM images of Ti6Al4V alloy polarized at 0.2 V vs. Ag/AgCl for 1-h in (a, d) 0.9% NaCl, (b, e) PBS, and (c, f) Hanks physiological solutions with 1 g L^{-1} BSA protein.

Table 3
Extracted Gaussian distribution parameters from the surface potential histograms in Fig. 7.

Region label	Constituents*	Mean value of surface potential (μ,mV)+ standard deviation (σ,mV)
Ti6Al4V alloy	α-phase	34.3 ± 12.5
	β-phase	48.5 ± 34.6
PBS+BSA	Protein cluster	40.5 ± 16.5
	Matrix (α and β-phase)	52.2 ± 9.4
Hanks+BSA	Protein+ α-phase	32.4 ± 11.8
	β-phase	39.6 ± 6.4
NaCl+BSA	α-phase	14.6 ± 7.1
	β-phase	18.7 ± 8.3
PBS+BSA+H_2O_2	α-phase	46.5 ± 12.2
	β-phase	54.1 ± 21.3
Hanks+BSA+H_2O_2	α-phase	34.7 ± 8.9
	β-phase	45.6 ± 8.5
NaCl+BSA+H_2O_2	α-phase	15.5 ± 6.5
	β-phase	19.8 ± 7.8

* The surface potential of α and β phases in BSA and BSA+H_2O_2 conditions is influenced by the adsorbed BSA.

a suitable adhesiveness level for improving fibroblast motility [76,77]. The molecular shape of the BSA protein is ellipsoidal, with dimensions of 4 nm × 4 nm × 14 nm [24]. Depending on the protein features and surface properties, the adsorption type of the BSA monolayer is side-on and end-on [18]. Stobiecka et al. [23] indicated that BSA on highly ordered pyrolytic graphite (HOPG) has a network morphology in comparison to a globular shape on Au because of the free diffusion and association into large assemblies with high self-interaction energies. Previous studies have shown that depending on the solid surface properties and environmental conditions, protein molecules can adsorb into co-operative adsorption with the growth of two-dimensional surface clusters that are densely ordered, leaving some uncovered regions, which is consistent with our SKPFM results [78,79].

The BSA protein in the Hanks' solution showed a finer network morphology in comparison with PBS media, whereas small regions with higher Volta potential correspond to the underlying β-phase grains that remain distinguishable. Based on image analysis, BSA proteins in PBS and Hanks' solution covered approximately 50% and 56% of the Ti6Al4V surface, respectively. Nevertheless, the BSA protein network in the Hanks' solution represented a smaller net size in the range from 200 nm to 5 µm, whereas the net size in the PBS solution was much larger, between 2 and 20 µm. Moreover, the protein regions in the PBS solution presented a higher surface potential (40.5 mV) than in those in Hanks' solution (32.4 mV), as reported in Table 3.

The PSD analysis (Fig. 8b) showed the heterogeneous distribution of the surface potential with respect to the spatial frequencies. The lowest and highest spatial frequencies were related to higher surface potential constituents (matrix, α-, and β-phases) and BSA proteins with lower surface potential distribution, respectively [37]. Two-dimensional PSD mappings (Fig. 8c) showed the surface potential distribution of various constituents (protein, α-, and β-phases) versus spatial frequencies in the x–y direction. By sweeping from fresh Ti6Al4V up to PBS, the homogeneous distribution on the surface potential at all frequencies, especially at high frequencies, decreased owing to the formation of large and dominant protein regions [80]. Indeed, the large circle in fresh Ti6Al4V represents the homogenous distribution of α- and β-phases with various surface potentials at different spatial frequencies. In the NaCl condition, a wider and more uniform distribution of surface potential of all con-

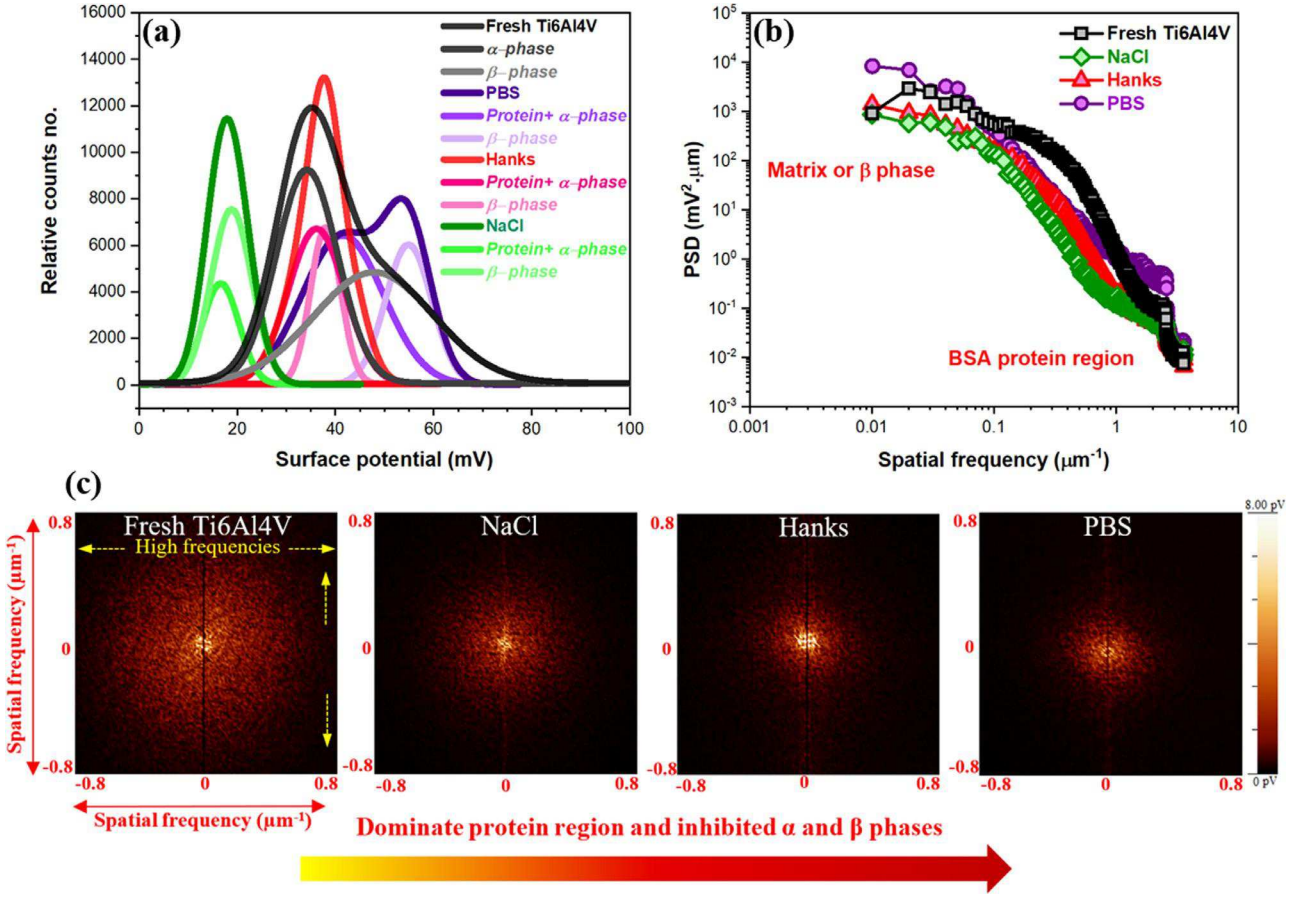

Fig. 8. (a) Surface potential histogram based in MGD, (b) PSD plots related to Fig. 7 and (c) 2D PSD maps of surface potential related to Fig. 7.

stituents was detected compared to the Hanks' solution and PBS with a small circle and semi-homogenous distribution of surface potential owing to the dominant BSA protein region that covered the matrix.

3.4.3. *Effect of the polarisation in the different environment containing BSA+H_2O_2*

The SKPFM maps of Ti6Al4V specimens after 1-h polarisation at 0.2 V vs. Ag/AgCl in the three base solutions containing BSA protein and H_2O_2 at 37 °C are shown in Fig. 9. The H_2O_2 agent significantly hindered the adsorption of BSA protein molecules on the surface, forming thick films in all environments to clearly detect the individual α- and β-phase grains. The surface potential values were slightly higher than those detected in solutions containing only BSA. Likewise, the total surface potential differences on the Ti6Al4V surface in the BSA+ H_2O_2 solutions followed the trend NaCl < Hanks' < PBS. To better observe the BSA features on the Ti6Al4V passivated surface, higher-magnification SKPFM images are shown in Fig. 9d–f.

As presented in the higher-magnification SKPFM images, higher surface coverage with BSA protein was noticed in Hanks' solution as compared to that in PBS solution, 51% and 40%, respectively. In addition, the morphology of the protein on the surface was different; in NaCl solution, the protein was in the form of aggregates (dark regions in Fig. 9d), whereas in PBS and Hanks' solutions, the protein presented a network morphology. As mentioned above, the primary adsorbed thin layer of phosphate and calcium-phosphate complex can provide appropriate conditions for BSA protein adsorption and control the migration and conformational arrangement of protein molecules. In comparison with the Volta potential maps obtained in solutions without H_2O_2, the adsorbed film seemed to be thinner as the β-phase regions with higher surface potential were still distinguishable.

As shown in Table 3, the α- and β-phases showed higher surface potentials in PBS solution (46.5 mV_{α} and 54.1 mV_{β}, respectively) than in the Hanks' and NaCl solutions, with values of 34.7 $mV_{\alpha/Hanks}$, 45.6 $mV_{\beta/Hanks}$ and 15.5 $mV_{\alpha/NaCl}$, 19.8 $mV_{\beta/NaCl}$, respectively.

3.5. *Degradation occurrence on complex oxide layer*

The particular morphological distribution of BSA protein and the differences in the surface potential could trigger localised corrosion. To investigate this, SEM micrographs at higher magnification of the marked areas in Fig. 7e are shown in Fig. 10a and b. Localised corrosion attacks (arrows) are observed at the interface protein/substrate interface owing to the formed crevices and the differences in the surface potential. This can be explained by various degradation mechanisms considering the metal ions releasing of metallic implants during interaction with proteins, especially human serum albumin (HAS) and BSA proteins as a consequence of (1) shielding effect or inhibiting the cathodic reaction, (2) attracting counterions, (3) a complexation process with the various oxide constituents, and (4) the Vroman effect, as presented schematically in Fig. 10c.

Some properties, such as the physiological environment and surface chemistry, have a direct effect on the degradation mechanism time. The shielding effect explains that the BSA protein initially decreases the release of metal ions by inhibiting the cathodic reactions on the passive film. However, with time (milliseconds to years), it provides a suitable condition for increasing the metal ion release process [9,44]. The BSA protein or BSA micronetwork/passive film interface is an attractive site for easier adsorption of the counterions (aggressive ions such as Cl^-). This can lead to penetration within the BSA protein layer and then into the BSA protein/passive film interface and finally promote lo-

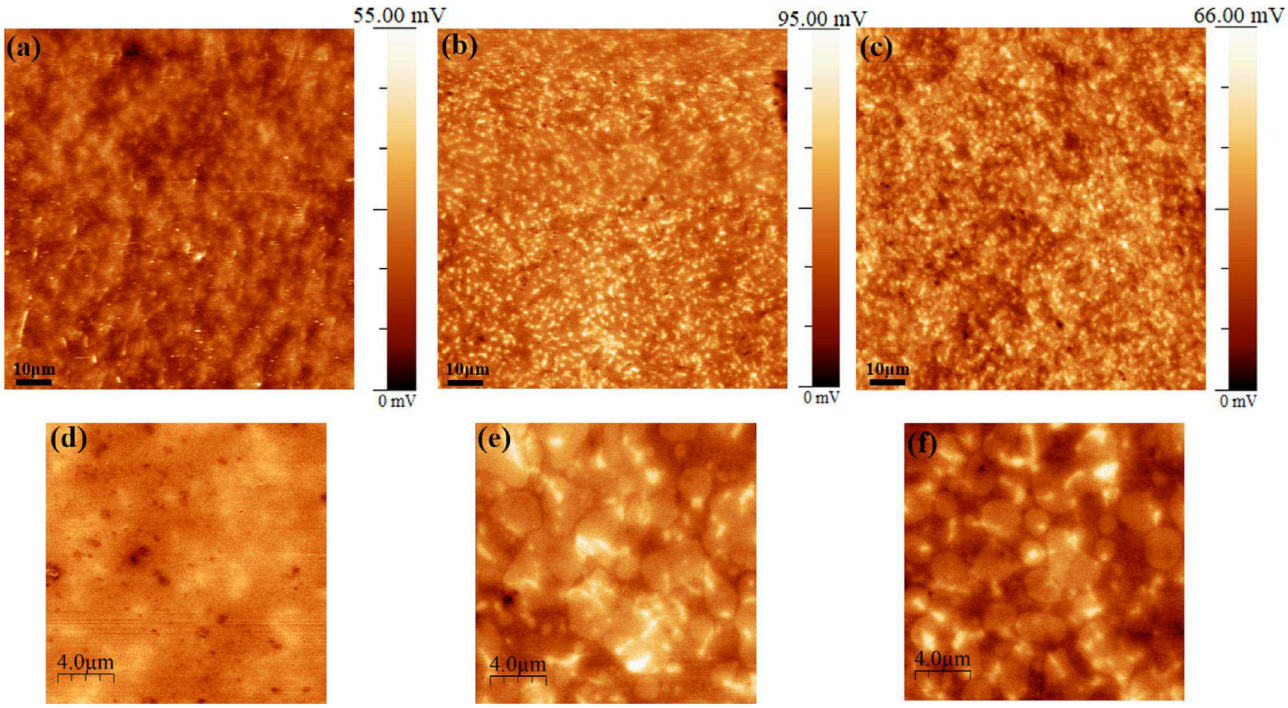

Fig. 9. Low and high magnification maps of surface potential of Ti6Al4V alloy polarized for 1-h at 0.2 V vs. Ag/AgCl in (a, d) NaCl, (b, e) PBS and (c, f) Hanks physiological solutions with 1 g L^{-1} BSA protein and 100 μM H_2O_2.

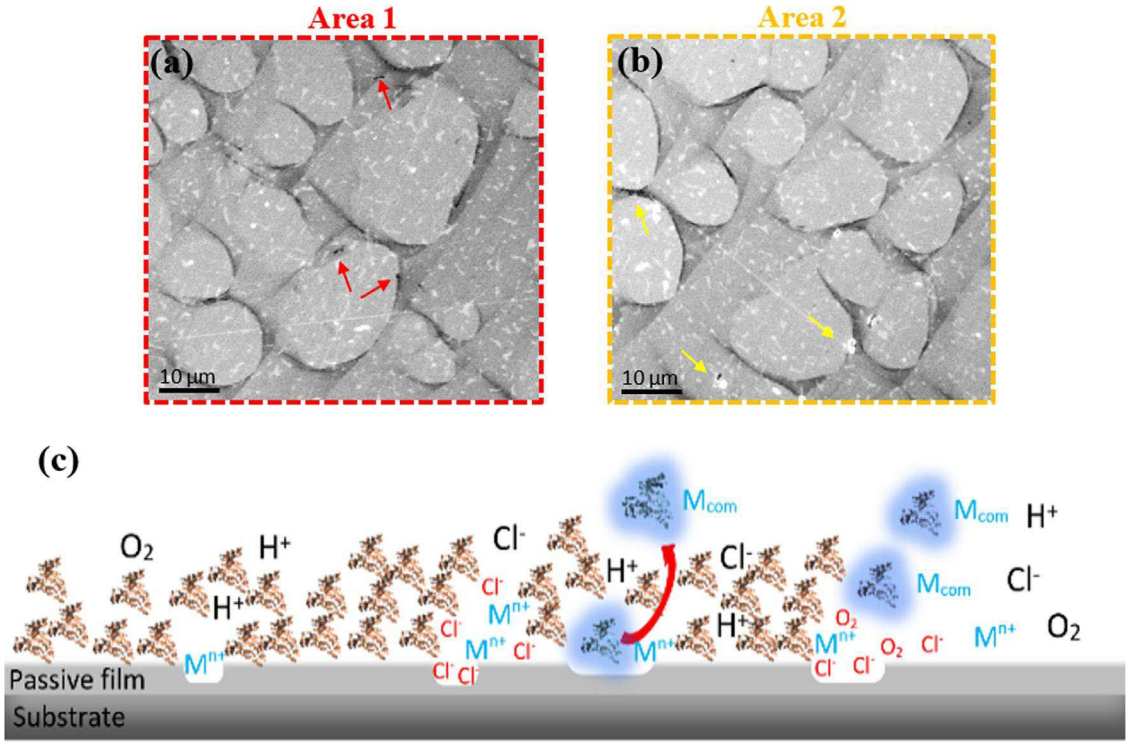

Fig. 10. (a and b) SEM images of adsorbed BSA protein on Ti6Al4V detected after 1-h polarisation at 0.2 V vs. Ag/AgCl in PBS solution containing 1 g L^{-1} BSA protein at 37 °C (marked areas in Fig. 7e, (c) Schematic representation of localized corrosion mechanism on passive metal in presence of BSA protein.

calised corrosion of the passive layer [35]. The BSA protein can create complexes with metal or metal–oxide species on passive films, which in turn triggers more degradation and formation of metal–protein conjugates [43]. The Vroman effect indicates that the detachment of metal–protein bounds is under the control of the exchange process of adsorbed proteins, which finally leads to enhancing the corrosion rate.

4. Conclusion

The present study contributes to an understanding of the role of different physiological solutions on the protein adsorption mechanism, distribution/morphology, and surface potential on α/β surface phases in Ti6Al4V using SKPFM, XPS, SEM, and electrochemical measurements.

The electrochemical measurements results indicated that the alloy is more resistant to corrosion in PBS solution in comparison to Hank's and NaCl. The addition of BSA leads to a slight increase of the corrosion current density and the passive current density in all tested solutions, whereas a more marked increase is observed by adding H_2O_2 or both BSA and H_2O_2. These results are correlated to the semiconductive character of the formed passive film. Indeed, Mott-Schottky analyses demonstrated that under inflammatory conditions (BSA+H_2O_2) an increase of the donor density of the passive film formed was noticed in all environments. XPS analyses and SKPFM maps revealed that specimens polarized in the NaCl environment containing BSA+H_2O_2 presented the highest protein covering, the lowest Ti and Al contents in the passive film and the lower surface potential compared to the other solutions. The morphology of the adsorbed protein changed from globular to a large micronetwork (PBS) to fine micro-nanonetworks (Hanks'), along with increasing the surface potential. According to the SKPFM and SEM images, the different interfaces including protein/α- or β-phases and the top surface of BSA protein were the susceptible sites for corrosion initiation owing to different surface potentials and suitable places for the adsorption of counter ions, e.g., Cl^-.

Summarizing the results of the electrochemical and surface analyses techniques it could be stated that the adsorption of protein on the surface of Ti6Al4V increases the degradation rate in all human body simulating solution and this effect is more intense in inflammatory conditions (presence of H_2O_2). On the other hand, the presence of phosphate and calcium species contributes to the formation of a more protective layer due to their adsorption on the alloy surface. This hinders the adsorption of BSA protein, decreasing the corrosion rate.

Declaration of Competing Interest

The authors declare that they have no known competing financial interests or personal relationships that could have appeared to influence the work reported in this paper.

Acknowledgments

This project has received funding from the European Union's Horizon 2020 research and innovation programme under the Marie Sklodowska-Curie grant agreement no. 764977.

References

[1] B. Sivaraman, K.P. Fears, R.A. Latour, Investigation of the effects of surface chemistry and solution concentration on the conformation of adsorbed proteins using an improved circular dichroism method, Langmuir 25 (5) (2009) 3050–3056.
[2] S. Karimi, T. Nickchi, A. Alfantazi, Effects of bovine serum albumin on the corrosion behaviour of AISI 316L, Co–28Cr–6Mo, and Ti–6Al–4V alloys in phosphate buffered saline solutions, Corros. Sci. 53 (10) (2011) 3262–3272.
[3] X. Quan, J. Liu, J. Zhou, Multiscale modeling and simulations of protein adsorption: progresses and perspectives, Curr. Opin. Colloid Interface Sci. (2018).
[4] Y.S. Hedberg, I. Dobryden, H. Chaudhary, Z. Wei, P.M. Claesson, C. Lendel, Synergistic effects of metal-induced aggregation of human serum albumin, Colloids Surf. B 173 (2019) 751–758.
[5] I. Van De Keere, R. Willaert, A. Hubin, J. Vereecken, Interaction of human plasma fibrinogen with commercially pure titanium as studied with atomic force microscopy and X-ray photoelectron spectroscopy, Langmuir 24 (5) (2008) 1844–1852.
[6] Y. Yan, H. Yang, Y. Su, L. Qiao, Albumin adsorption on CoCrMo alloy surfaces, Sci. Rep. 5 (2015) 18403.
[7] S. Guo, D. Pranantyo, E.-T. Kang, X.J. Loh, X. Zhu, D. Jańczewski, K.G. Neoh, Dominant albumin–surface interactions under independent control of surface charge and wettability, Langmuir 34 (5) (2018) 1953–1966.
[8] P. Roach, D. Farrar, C.C. Perry, Interpretation of protein adsorption: surface-induced conformational changes, J. Am. Chem. Soc. 127 (22) (2005) 8168–8173.
[9] Y.S. Hedberg, Role of proteins in the degradation of relatively inert alloys in the human body, npj Mater. Degrad. 2 (1) (2018) 26.
[10] A. Hasan, V. Saxena, L.M. Pandey, Surface functionalization of Ti6Al4V via self-assembled monolayers for improved protein adsorption and fibroblast adhesion, Langmuir 34 (11) (2018) 3494–3506.
[11] R. Tsaryk, M. Kalbacova, U. Hempel, D. Scharnweber, R.E. Unger, P. Dieter, C.J. Kirkpatrick, K. Peters, Response of human endothelial cells to oxidative stress on Ti6Al4V alloy, Biomaterials 28 (5) (2007) 806–813.
[12] F. Yu, O. Addison, A.J. Davenport, A synergistic effect of albumin and H_2O_2 accelerates corrosion of Ti6Al4V, Acta Biomater. 26 (2015) 355–365.
[13] W. Xu, F. Yu, L. Yang, B. Zhang, B. Hou, Y. Li, Accelerated corrosion of 316L stainless steel in simulated body fluids in the presence of H_2O_2 and albumin, Mater. Sci. Eng. 92 (2018) 11–19.
[14] J.-L. Wang, R. Liu, T. Majumdar, S. Mantri, V. Ravi, R. Banerjee, N. Birbilis, A closer look at the in vitro electrochemical characterisation of titanium alloys for biomedical applications using in-situ methods, Acta Biomater. 54 (2017) 469–478.
[15] S. Takemoto, M. Hattori, M. Yoshinari, E. Kawada, Y. Oda, Corrosion behavior and surface characterization of titanium in solution containing fluoride and albumin, Biomaterials 26 (8) (2005) 829–837.
[16] J.P. Bearinger, C.A. Orme, J.L. Gilbert, In situ imaging and impedance measurements of titanium surfaces using AFM and SPIS, Biomaterials 24 (11) (2003) 1837–1852.
[17] T.M. Cotton, J.H. Kim, G.D. Chumanov, Application of surface-enhanced Raman spectroscopy to biological systems, J. Raman Spectrosc. 22 (12) (1991) 729–742.
[18] I. Ron, L. Sepunaru, S. Itzhakov, T. Belenkova, N. Friedman, I. Pecht, M. Sheves, D. Cahen, Proteins as electronic materials: Electron transport through solid-state protein monolayer junctions, J. Am. Chem. Soc. 132 (12) (2010) 4131–4140.
[19] T. Guckeisen, S. Hosseinpour, W. Peukert, Isoelectric points of proteins at the air/liquid interface and in solution, Langmuir (2019).
[20] A. Sethuraman, M. Han, R.S. Kane, G. Belfort, Effect of surface wettability on the adhesion of proteins, Langmuir 20 (18) (2004) 7779–7788.
[21] F.A. Denis, P. Hanarp, D.S. Sutherland, J. Gold, C. Mustin, P.G. Rouxhet, Y.F. Dufrêne, Protein adsorption on model surfaces with controlled nanotopography and chemistry, Langmuir 18 (3) (2002) 819–828.
[22] M.H. Wood, C.G. Payagalage, T. Geue, Bovine serum albumin and fibrinogen adsorption at the 316L stainless steel/aqueous interface, J. Phys. Chem. B 122 (19) (2018) 5057–5065.
[23] M. Stobiecka, M. Hepel, J. Radecki, Transient conformation changes of albumin adsorbed on gold piezoelectrodes, Electrochim. Acta 50 (25–26) (2005) 4873–4887.
[24] B. Jachimska, K. Tokarczyk, M. Łapczyńska, A. Puciul-Malinowska, S. Zapotoczny, Structure of bovine serum albumin adsorbed on silica investigated by quartz crystal microbalance, Colloids Surf. A 489 (2016) 163–172.
[25] H.-H. Huang, Effect of fluoride and albumin concentration on the corrosion behavior of Ti–6Al–4V alloy, Biomaterials 24 (2) (2003) 275–282.
[26] W. Huo, L. Zhao, W. Zhang, J. Lu, Y. Zhao, Y. Zhang, In vitro corrosion behavior and biocompatibility of nanostructured Ti6Al4V, Mater. Sci. Eng. 92 (2018) 268–279.
[27] F. Contu, B. Elsener, H. Böhni, A study of the potentials achieved during mechanical abrasion and the repassivation rate of titanium and Ti6Al4V in inorganic buffer solutions and bovine serum, Electrochim. Acta 50 (1) (2004) 33–41.
[28] X. Cheng, S.G. Roscoe, Corrosion behavior of titanium in the presence of calcium phosphate and serum proteins, Biomaterials 26 (35) (2005) 7350–7356.
[29] C. Barth, A.S. Foster, C.R. Henry, A.L. Shluger, Recent trends in surface characterization and chemistry with high-resolution scanning force methods, Adv. Mater. 23 (4) (2011) 477–501.
[30] V. Palermo, A. Liscio, M. Palma, M. Surin, R. Lazzaroni, P. Samorì, Exploring nanoscale electrical and electronic properties of organic and polymeric functional materials by atomic force microscopy based approaches, Chem. Commun. (32) (2007) 3326–3337.
[31] E. Rahimi, A. Rafsanjani-Abbasi, A. Imani, S. Hosseinpour, A. Davoodi, Correlation of surface Volta potential with galvanic corrosion initiation sites in solid-state welded Ti-Cu bimetal using AFM-SKPFM, Corros. Sci. 140 (2018) 30–39.
[32] E. Rahimi, A. Rafsanjani-Abbasi, A. Imani, A. Davoodi, TiO_2/Cu_2O coupled oxide films in Cl– ion containing solution: Volta potential and electronic properties characterization by scanning probe microscopy, Mater. Chem. Phys. 212 (2018) 403–407.
[33] B. Moores, F. Hane, L. Eng, Z. Leonenko, Kelvin probe force microscopy in application to biomolecular films: frequency modulation, amplitude modulation, and lift mode, Ultramicroscopy 110 (6) (2010) 708–711.
[34] A.K. Sinensky, A.M. Belcher, Label-free and high-resolution protein/DNA nanoarray analysis using Kelvin probe force microscopy, Nat. Nanotechnol. 2 (10) (2007) 653.
[35] C. Leung, H. Kinns, B.W. Hoogenboom, S. Howorka, P. Mesquida, Imaging surface charges of individual biomolecules, Nano Lett. 9 (7) (2009) 2769–2773.
[36] R. Ovarfort, New electrochemical cell for pitting corrosion testing, Corros. Sci. 28 (2) (1988) 135–140.
[37] Z. Esfahani, E. Rahimi, M. Sarvghad, A. Rafsanjani-Abbasi, A. Davoodi, Correlation between the histogram and power spectral density analysis of AFM and SKPFM images in an AA7023/AA5083 FSW joint, J. Alloy. Compd. 744 (2018) 174–181.
[38] P. Dash, P. Mallick, H. Rath, A. Tripathi, J. Prakash, D. Avasthi, S. Mazumder, S. Varma, P. Satyam, N. Mishra, Surface roughness and power spectral density study of SHI irradiated ultra-thin gold films, Appl. Surf. Sci. 256 (2) (2009) 558–561.
[39] M. Flemming, L. Coriand, A. Duparré, Ultra-hydrophobicity through stochastic surface roughness, J. Adhes. Sci. Technol. 23 (3) (2009) 381–400.
[40] S. Karimi, A. Alfantazi, Electrochemical corrosion behavior of orthopedic biomaterials in presence of human serum albumin, J. Electrochem. Soc. 160 (6) (2013) C206–C214.
[41] M. Aziz-Kerrzo, K.G. Conroy, A.M. Fenelon, S.T. Farrell, C.B. Breslin, Electrochemical studies on the stability and corrosion resistance of titanium-based implant materials, Biomaterials 22 (12) (2001) 1531–1539.
[42] I. Milošev, CoCrMo alloy for biomedical applications, in: Biomedical Applications, Springer, 2012, pp. 1–72.
[43] A.I. Muñoz, S. Mischler, Interactive effects of albumin and phosphate ions on the corrosion of CoCrMo implant alloy, J. Electrochem. Soc. 154 (10) (2007) C562–C570.
[44] M. Talha, Y. Ma, P. Kumar, Y. Lin, A. Singh, Role of protein adsorption in the bio corrosion of metallic implants–a review, Colloids Surf. B (2019).
[45] T. Hanawa, S. Hiromoto, K. Asami, Characterization of the surface oxide film of a Co–Cr–Mo alloy after being located in quasi-biological environments using XPS, Appl. Surf. Sci. 183 (1–2) (2001) 68–75.

[46] J.E. Ellingsen, A study on the mechanism of protein adsorption to TiO_2, Biomaterials 12 (6) (1991) 593–596.
[47] J. Pan, D. Thierry, C. Leygraf, Electrochemical impedance spectroscopy study of the passive oxide film on titanium for implant application, Electrochim. Acta 41 (7–8) (1996) 1143–1153.
[48] J. Pan, D. Thierry, C. Leygraf, Hydrogen peroxide toward enhanced oxide growth on titanium in PBS solution: blue coloration and clinical relevance, J. Biomed. Mater. Res. 30 (3) (1996) 393–402.
[49] C. Fonseca, M. Barbosa, Corrosion behaviour of titanium in biofluids containing H_2O_2 studied by electrochemical impedance spectroscopy, Corros. Sci. 43 (3) (2001) 547–559.
[50] Y. Zhang, O. Addison, F. Yu, B.C.R. Troconis, J.R. Scully, A.J. Davenport, Time-dependent enhanced corrosion of Ti6Al4V in the presence of H_2O_2 and albumin, Sci. Rep. 8 (1) (2018) 3185.
[51] S.L. de Assis, S. Wolynec, I. Costa, Corrosion characterization of titanium alloys by electrochemical techniques, Electrochim. Acta 51 (8–9) (2006) 1815–1819.
[52] X. Cheng, Y. Wang, C. Dong, X. Li, The beneficial galvanic effect of the constituent phases in 2205 duplex stainless steel on the passive films formed in a 3.5% NaCl solution, Corros. Sci. 134 (2018) 122–130.
[53] N. Hakiki, M.D.C. Belo, A. Simoes, M. Ferreira, Semiconducting properties of passive films formed on stainless steels influence of the alloying elements, J. Electrochem. Soc. 145 (11) (1998) 3821–3829.
[54] A.E. Nel, L. Mädler, D. Velegol, T. Xia, E.M. Hoek, P. Somasundaran, F. Klaessig, V. Castranova, M. Thompson, Understanding biophysicochemical interactions at the nano–bio interface, Nat. Mater. 8 (7) (2009) 543–557.
[55] A. Fattah-Alhosseini, O. Imantalab, G. Ansari, The role of grain refinement and film formation potential on the electrochemical behavior of commercial pure titanium in Hank's physiological solution, Mater. Sci. Eng. 71 (2017) 827–834.
[56] G. Ansari, A. Fattah-alhosseini, On the passive and semiconducting behavior of severely deformed pure titanium in Ringer's physiological solution at 37 C: a trial of the point defect model, Mater. Sci. Eng. 75 (2017) 64–71.
[57] D.D. Macdonald, The point defect model for the passive state, J. Electrochem. Soc. 139 (12) (1992) 3434.
[58] H. Krawiec, V. Vignal, E. Schwarzenboeck, J. Banas, Role of plastic deformation and microstructure in the micro-electrochemical behaviour of Ti–6Al–4V in sodium chloride solution, Electrochim. Acta 104 (2013) 400–406.
[59] L.N. Wang, A. Shinbine, J.L. Luo, Electrochemical behavior of CoCrMo implant in Ringer's solution, Surf. Interface Anal. 45 (9) (2013) 1323–1328.
[60] O.R. Cámara, L.B. Avalle, F.Y. Oliva, Protein adsorption on titanium dioxide: effects on double layer and semiconductor space charge region studied by EIS, Electrochim. Acta 55 (15) (2010) 4519–4528.
[61] S. Karimi, T. Nickchi, A.M. Alfantazi, Long-term corrosion investigation of AISI 316L, Co–28Cr–6Mo, and Ti–6Al–4V alloys in simulated body solutions, Appl. Surf. Sci. 258 (16) (2012) 6087–6096.
[62] Y.S. Hedberg, M. Žnidaršič, G. Herting, I. Milošev, I. Odnevall Wallinder, Mechanistic insight on the combined effect of albumin and hydrogen peroxide on surface oxide composition and extent of metal release from Ti6Al4V, J. Biomed. Mater. Res. Part B 107 (3) (2019) 858–867.
[63] Y. Tsutsumi, D. Nishimura, H. Doi, N. Nomura, T. Hanawa, Difference in surface reactions between titanium and zirconium in Hanks' solution to elucidate mechanism of calcium phosphate formation on titanium using XPS and cathodic polarization, Mater. Sci. Eng. 29 (5) (2009) 1702–1708.
[64] B. Wu, C. Mu, G. Zhang, W. Lin, Effects of Cr^{3+} on the structure of collagen fiber, Langmuir 25 (19) (2009) 11905–11910.
[65] K. Hamada, M. Kon, T. Hanawa, K.i. Yokoyama, Y. Miyamoto, K. Asaoka, Hydrothermal modification of titanium surface in calcium solutions, Biomaterials 23 (10) (2002) 2265–2272.
[66] E. Chang, T.-M. Lee, Effect of surface chemistries and characteristics of Ti6Al4V on the Ca and P adsorption and ion dissolution in Hank's ethylene diamine tetra-acetic acid solution, Biomaterials 23 (14) (2002) 2917–2925.
[67] P. Tengvall, H. Elwing, I. Lundström, Titanium gel made from metallic titanium and hydrogen peroxide, J. Colloid Interface Sci. 130 (2) (1989) 405–413.
[68] Y.-S. Hsu, E. Chang, H.-S. Liu, Hydrothermally-grown monetite ($CaHPO_4$) on hydroxyapatite, Ceram. Int. 24 (4) (1998) 249–254.
[69] D. Briggs, Practical surface analysis, Auger X-Ray Photoelectron. Spectrosc. 1 (1990) 151–152.
[70] E. Rahimi, A. Rafsanjani-Abbasi, A. Davoodi, S. Hosseinpour, Characterization of the native passive film on ferrite and austenite phases of sensitized 2205 duplex stainless steel, J. Electrochem. Soc. 166 (16) (2019) C609–C616.
[71] D. Nakhaie, A. Davoodi, G.R. Ebrahimi, The Influence of cold plastic deformation on passivity of Ti-6Al-4V alloy studied by electrochemical and local probing techniques, Corrosion 72 (1) (2015) 110–118.
[72] P. Davis, K. Robles, K. Livingston, S. Johns, V. Ravi, E. Graugnard, M. Hurley, Phase separation in Ti-6Al-4V alloys with boron additions for biomedical applications: scanning kelvin probe force microscopy investigation of microgalvanic couples and corrosion initiation, JOM 69 (8) (2017) 1446–1454.
[73] H.B. Michaelson, The work function of the elements and its periodicity, J. Appl. Phys. 48 (11) (1977) 4729–4733.
[74] J.-W. Park, K.-B. Park, J.-Y. Suh, Effects of calcium ion incorporation on bone healing of Ti6Al4V alloy implants in rabbit tibiae, Biomaterials 28 (22) (2007) 3306–3313.
[75] M. Salerno, S. Dante, Scanning Kelvin probe microscopy: challenges and perspectives towards increased application on biomaterials and biological samples, Materials 11 (6) (2018) 951.
[76] F. Bathawab, M. Bennett, M. Cantini, J. Reboud, M.J. Dalby, M. Salmerón-Sánchez, Lateral chain length in polyalkyl acrylates determines the mobility of fibronectin at the cell/material interface, Langmuir 32 (3) (2016) 800–809.
[77] N.B. Guerra, C. González-García, V. Llopis, J.C. Rodríguez-Hernández, D. Moratal, P. Rico, M. Salmerón-Sánchez, Subtle variations in polymer chemistry modulate substrate stiffness and fibronectin activity, Soft Matter 6 (19) (2010) 4748–4755.
[78] M. Rabe, D. Verdes, S. Seeger, Understanding protein adsorption phenomena at solid surfaces, Adv. Colloid Interface Sci. 162 (1–2) (2011) 87–106.
[79] A.P. Minton, Effects of excluded surface area and adsorbate clustering on surface adsorption of proteins. II. Kinetic models, Biophys. J. 80 (4) (2001) 1641–1648.
[80] H.-G. Park, H.-C. Jeong, Y.H. Jung, D.-S. Seo, Control of the wrinkle structure on surface-reformed poly (dimethylsiloxane) via ion-beam bombardment, Sci. Rep. 5 (2015) 12356.